



1 **Integration of microseism, wavemeter buoy, HF Radar and hindcast data to analyze the**
2 **Mediterranean cyclone Helios**

3

4 **Alfio Marco Borzi^{1*}, Vittorio Minio¹, Raphael De Plaen², Thomas Lecocq², Salvatore**
5 **Alparone³, Salvatore Aronica⁴, Flavio Cannavò³, Fulvio Capodici⁵, Giuseppe Ciralo⁵,**
6 **Sebastiano D'Amico⁶, Danilo Contrafatto³, Giuseppe Di Grazia³, Ignazio Fontana⁴,**
7 **Giovanni Giacalone⁴, Graziano Larocca³, Carlo Lo Re⁷, Giorgio Manno⁵, Gabriele**
8 **Nardone⁷, Arianna Orasi⁷, Marco Picone⁷, Giovanni Scicchitano⁸, Andrea Cannata^{1,3}**

9 ¹Dipartimento di Scienze Biologiche, Geologiche ed Ambientali - Sezione di Scienze della Terra, Università degli
10 Studi di Catania, Catania, Italy;

11 ²Seismology-Gravimetry, Royal Observatory of Belgium, Brussel, Belgium;

12 ³Istituto Nazionale di Geofisica e Vulcanologia - Sezione di Catania, Osservatorio Etneo, Catania, Italy;

13 ⁴Institute of Anthropic Impacts and Sustainability in the Marine Environment - National Research Council (IAS-
14 CNR), Campobello di Mazara, TP, Italy

15 ⁵Dipartimento di Ingegneria Civile, Ambientale, Aerospaziale, dei Materiali, University of Palermo, 90128
16 Palermo, Italy

17 ⁶Department of Geosciences, University of Malta, Msida, Malta;

18 ⁷Centro Nazionale per la Caratterizzazione Ambientale e la Protezione Della Fascia Costiera, la Climatologia
19 Marina e l'Oceanografia Operativa, Italian National Institute for Environmental Protection and Research, Rome,
20 Italy.

21 ⁸Dipartimento di Scienze della Terra e Geoambientali, Università degli Studi di Bari Aldo Moro, 70125 Bari, Italy

22 *Corresponding author

23 alfio.borzi@phd.unict.it

24 Corso Italia 57, 95129 Catania (Italy)

25



26 **Keywords:** Microseism, wavemeter buoy, HF Radar, Mediterranean cyclones, climate change,
27 monitoring sea state

28 **Abstract**

29 In this work, we study a Mediterranean cyclone, ~~that was~~ called Helios ~~and~~ took place during
30 the period 9-11 February 2023 in the southeastern part of Sicily and Malta Island, by a
31 multiparametric approach combining microseism results with sea state and meteorological data
32 provided by wavemeter buoy, HF Radar, hindcast maps and satellite SEVIRI images. The sub-
33 tropical system Helios caused heavy rainfall, strong wind gusts and violent storm surges with
34 significant wave heights greater than 5 meters. We deal with the relationships between such a
35 system and the features of microseism (the most continuous and ubiquitous seismic signal on
36 the Earth) in terms of spectral content, space-time variation of the amplitude and source
37 locations tracked by means of two different methods (amplitude-based grid search and array
38 techniques). By comparing the location of the microseism sources and the area affected by
39 significant storm surges, derived from sea state data, we note that the microseism location
40 results are in agreement with the real position of the storm surges. In addition, we are able to
41 obtain the seismic signature of Helios using a method that exploits the coherence of continuous
42 seismic noise. Hence, we show how an innovative monitoring system of the Mediterranean
43 cyclones can be designed by integrating microseism information with other techniques
44 routinely used to study meteorological phenomena.

45

46 **1. Introduction**

47 Significant storm surges driven by intense low-pressure systems represent one of the main
48 hazards to the Mediterranean coastal areas causing flooding, beach erosion and damage to
49 infrastructures and cultural heritages (Flaounas et al., 2022; Lionello et al., 2019;).
50 Occasionally, when there are favorable conditions like high sea temperature and high contrast



51 of temperature sea-air, the cyclones can acquire the characteristics of a MEDiterranean
52 hurriCANE (hereinafter Medicane). Medicanes genesis is favored when an extratropical
53 depression gets isolated from the polar jet stream. The "cut-off" feature, when situated above
54 the Mediterranean Sea, remains relatively stable and takes advantage of the abundant heat and
55 humidity from the sea to generate organized convection (Faranda et al., 2022).

56 The structure of a Medicane is characterized by the presence of a central free-cloud "eye", a
57 strong rotation around the pressure minimum, an eyewall with convective cells, from which
58 rain bands extend. It can be considered like a small-scale tropical cyclone and can lead to sea-
59 level rise, storm surge and sea waves that can reach significant heights of about five meters
60 (Miglietta and Rotunno, 2019). The typical Medicane lifetime is limited to a few days,
61 generally from 2 to 5 days, as a result of the small areal extension of the Mediterranean Sea
62 that represents their main energy source; for the same reason also the diameter is generally
63 restricted to a range between 100 and 300 km (Comellas et al., 2021), and their intensity rarely
64 exceeds the category 1 of the Saffir-Simpson hurricane wind scale (Miglietta end Rotunno.,
65 2019). In addition, due to the geometrical and meteorological characteristics of the
66 Mediterranean Sea, a Medicane reaches fully tropical characteristics (a symmetric, deep warm-
67 core structure and convection in their development and maintenance) for a short time, while
68 extratropical features (non-symmetrical structure and not well-developed convection around
69 the core) prevail for most of their lifetime (Miglietta et al., 2011, 2013). There is no clear
70 separation between tropical and extratropical cyclones, the first approach to differentiate these
71 cyclones was developed by Hart (2003). This method, called cyclone phase space analysis,
72 relies on a large spectrum of different cyclone types in a way to form a continuum between
73 tropical and extratropical cyclones.

74 The favorable months to the Medicanes generations are the autumn and early winter months
75 (from September to January). Indeed during these months, the Mediterranean Sea preserves



76 high temperatures after the summer season, and the first cold upper-air troughs are observed,
77 thus creating a high sea-air temperature gradient (Cavicchia et al., 2014; Nastos et al., 2018).
78 Specifically, the occurrence of intense convective instability is initiated when the polar jet
79 stream transports cold air masses over the warmer Mediterranean Sea (Cavicchia et al., 2014;
80 Nastos et al., 2018). The Medicanes generation during the late-winter months (February and
81 March) is possible but less common (Cavicchia et al., 2014, Tous and Romero, 2013).
82 These Mediterranean extreme weather events caused damages, floods, deaths, and injuries in
83 several Mediterranean coastal areas (South France, Central and South Italy, Malta, Balearic
84 islands, Greece, Crete, Turkey, and some African states; Androulidakis et al., 2022; Bouin and
85 Brossier, 2020; Carrió et al., 2017; Dafis et al., 2018; Di Muzio et al., 2019; Faranda et al.,
86 2022; Kerkmann and Bachmeier, 2011; Lagouvardos et al., 2022; Pravia-Sarabia et al., 2021;
87 Portmann et al., 2020; Rumora et al., 2018; Varlas et al., 2020; Zimbo et al., 2022). As
88 explained by Cavicchia et al. (2014), the most frequent genesis regions are the Balearic Islands
89 and the Ionian Sea. In particular, during the last 12 years, the majority of the Medicanes have
90 been developed over the Ionian Sea and this is probably linked to the sea surface temperature
91 that, as shown by Shaltout and Omstedt (2014), in the Ionian Sea is constantly 1.0°-1.5° C
92 higher than that in the Tyrrhenian Sea.

93 Although these extreme Mediterranean events showed significant wave heights (hereinafter
94 SWH, defined as the average wave height of the highest one-third of the waves), comparable
95 to the common seasonal storms, they caused greater coastal flooding (Scardino et al., 2022;
96 Scicchitano et al., 2021). The strong winds, generated during a Medicane, cause the
97 development of powerful wave motions and lead to an energy transfer from the sea waves to
98 the solid Earth (Borzi et al., 2022). This energy transfer between the atmosphere, the
99 hydrosphere and the solid Earth is one of the generation mechanisms of the most continuous
100 and ubiquitous seismic signal on the Earth, called microseism (e.g. Hasselmann, 1963;



101 Longuet-Higgins, 1950). In connection with the spectral content and the source mechanism
102 (e.g. Haubrich and McCamy, 1969), it is possible to divide this signal into: **primary microseism**
103 **(PM), that shows the same period as the oceanic waves (13 - 20 s) and low amplitudes, and is**
104 **generated by the energy transfer of oceanic waves breaking against the shoreline (Ardhuin et**
105 **al., 2015; Hasselmann, 1963);** secondary microseism (SM), generated by sea waves with the
106 same frequency traveling in opposite directions and exhibiting frequency about twice of the
107 frequency of the oceanic waves (period of 5 - 10 s) and amplitude higher than the PM (e.g.
108 Ardhuin and Roland, 2012; Ardhuin et al., 2015; Longuet-Higgins, 1950; Oliver and Page,
109 1963); short-period secondary microseism (SPSM), that has a period shorter than 5 seconds
110 and is generated by the interaction between local wave motions near the coastline (Bromirski
111 et al., 2005).

112 Several works deal with the relationship between microseism and the sea state (Ardhuin et al.,
113 2019; Cannata et al., 2020; Guerin et al., 2022; Moschella et al., 2020), while others take into
114 account specifically the relationship between microseism and cyclonic activity (e.g.,
115 Bromirski, 2001; Bromirski et al., 2005; Gerstoft et al., 2006; Gualtieri et al., 2018; Lin et al.,
116 2017; Retailleau and Gualtieri, 2019, 2021; Zhang et al., 2010) considering in particular
117 typhoons (Lin et al., 2017), tropical cyclones (Zhang et al., 2010), and hurricanes (Gerstoft et
118 al., 2006). Interestingly, Bromirski (2001) and Bromirski et al. (2005) showed that the
119 microseism bands most affected by the presence of a cyclone are the SM and SPSM ones.

120 For the first time, the relationship between SM, SPSM, and Mediane was analyzed by Borzi
121 et al. (2022), who considered the Mediane Apollo to reconstruct both the seismic variation in
122 terms of power spectral density (PSD) and root mean square (RMS) amplitude and the Mediane
123 position during its lifetime by two different methods (array analysis and grid search method by
124 means of seismic amplitude decay). In this work, we explore the relationship between
125 microseism and the Sub-Tropical system “Helios” that occurred in the Sicily Channel during



126 the period 9-11 February 2023 (**Figure 1**). The microseism results are integrated with
127 wavemeter buoy, HF Radar, hindcast and satellite data (SEVIRI Images) to perform an
128 investigation as comprehensive as possible of this extreme Mediterranean meteo-marine event.

129 **2. Sub-tropical system “Helios” (9-11 February 2023)**

130 During the period 9-11 February 2023, a low-pressure system, later renamed Helios, developed
131 over the Sicily Channel due to the strong contrast between the very cold air, coming from NE
132 (Balkans area) and the relatively warm sea surface. From satellite data, the warm core anomaly
133 of this cyclone is evident, requisite for the development of the Medicane. However, this storm
134 failed to become a Medicane, for which it is necessary that the cyclone maintains well-
135 developed convection around the eye, absent in this case probably due to a little interaction
136 between sea-air caused by sea surface temperature not suitable for the development of a
137 Medicane (<https://twitter.com/medcyclones/status/1623795373423620096?s=20>,
138 <https://twitter.com/medcyclones/status/1623992335104081921?s=20>,
139 <https://twitter.com/medcyclones/status/1624143740800536591?s=20>, last access 23/05/2023).

140 In spite of this, Helios, thanks to its proximity to the Sicilian and Maltese coasts, was able to
141 produce damage along these areas. The effects of the sub-tropical system Helios were
142 significant, especially in Catania, Ragusa and Siracusa provinces (located in the south-eastern
143 part of Sicily), where the Sicilian Meteorological service (“Regione Siciliana—SIAS—
144 Servizio Informativo Agrometeorologico Siciliano”, <http://www.sias.regione.sicilia.it/>)
145 recorded heavy rainfall, more than 200 mm/48 h and peaks of about 500 mm/48 h near Noto
146 for the days 9-10 February 2023, heavy snowfall starting from 1200 m a.s.l. with accumulations
147 of fresh snow on Etna thicker than two meters, strong wind gusts up to 90 km/h along the
148 exposed coast (Davies, 2023) and severe storm surge with SWH greater than 5 meters. Similar
149 effects were also recorded in Malta. The minimum pressure value in the cyclone eye amounted



150 to 1002 hPa. An overview of the positions and the extension of the sub-tropical system Helios
151 is represented in **Figure 1**.

152 As a consequence of the damage caused by Helios, the Regional Sicilian Government decided
153 to require a national state of emergency for 12 months for all the municipalities of Catania,
154 Siracusa, and Ragusa provinces and some municipalities of Messina province
155 (https://www2.regione.sicilia.it/deliberegiunta/file/giunta/allegati/N.099_15.02.2023.pdf, last
156 access 23/05/2023).

157

158 **3. Data and Methods**

159 We analyzed the data recorded in the period 8 to 13 February 2023 comprising the development
160 of Helios, the climax in terms of minimum pressure value, wind velocity, precipitation intensity
161 and SWH, and its decline.

162 **3.1. Seismic data**

163 We used 105 seismic stations installed along the Italian and French coastal areas, in the Sicily
164 channel coastlines (in Malta, Lampedusa and Linosa islands), in Corsica island and along the
165 Greek coastal areas to perform spectral analysis, localization analysis by the grid search method
166 based on seismic amplitude decay and to obtain the seismic signature of the analyzed event
167 (**Figure 2a** and **Supplementary Table 1**). Additionally, 15 seismic stations, installed in the
168 Etnean area, were used to conduct array analysis (**Figure 2b** and **Supplementary table 2**). The
169 selected seismic stations show specific characteristics: they are i) installed near the coastal
170 areas and ii) equipped with 3-component broadband seismic sensors.

171 **3.2. Sea state measures**

172 In this work, we use sea state data derived from four independent methodologies. In particular,
173 we used: i) significant wave height (SWH-Hind), provided by the hindcast maps produced by



174 Copernicus; ii) significant wave height (SWH-Buoy), period and direction of the waves
175 measured by the wavemeter buoy installed near Mazara del Vallo; iii) significant wave height
176 (SWH-HF), period and direction of the waves obtained by the HF Radar installed at the Marina
177 di Ragusa harbor; iv) SEVIRI Images to spatially and temporally track the position of the
178 cyclone. These four different data sources have been used to both describe the sea state
179 evolution during the Helios event, and characterize the physical state of the sea which is strictly
180 correlated to the microseism derived outputs.

181 **3.2.1. Copernicus Data**

182 Regarding the description of the Helios event in terms of spatio/temporal distribution of SWH,
183 wave period and direction over the whole domain, we referred to the
184 “MEDSEA_HINDCAST_WAV_006_012” product, provided by the Copernicus Marine
185 Environment Monitoring Service (CMEMS) (Korres et al., 2019). The CMEMS product
186 contains the hindcast maps of the Mediterranean Sea Waves forecasting system and is based
187 on the third-generation wave model WAM Cycle 4.5.4 composed by hourly wave parameters
188 at 1/24° horizontal resolution (Korres et al., 2019).

189 **3.2.2 Wavemeter buoy data**

190 Concerning the wave buoy, in **Figure 2c** we show the locations of this buoy, located offshore
191 of Mazara del Vallo, at a depth of 85 m. The Mazara buoy is managed by ISPRA and is part of
192 the National Wave Buoy Network (RON). The instrumental equipment consists of buoys
193 allowing the acquisition of wave parameters in real time. The long time series represent an
194 important heritage for the knowledge of marine phenomena affecting the Italian seas, both in
195 terms of climatology and extreme events. The RON National Wave Network is now composed
196 of 7 stations located off the Italian coasts for the continuous measurement of wave and
197 meteorological parameters, such as wind direction and speed, atmospheric pressure, water



198 surface and air temperatures, with real-time data transmission. Until 2014, the ISPRA wave
199 buoy network was equipped with WatchKeeper™ weather wave meters manufactured by the
200 Canadian company AXYS Ltd. (Bencivenga et al., 2012). The new meteo-marine buoys were
201 developed, designed and built in Italy for the specific needs of ISPRA. Data are collected
202 continuously for periods of 20-25 minutes and are provided every 30 minutes.

203 The parameters recorded by the wavemeter buoy and used in this study are: i) SWH (m), ii)
204 wave mean period (s) and iii) wave mean direction (°).

205 **3.2.3. HF Radar data**

206 Sea state measures are also provided by the HF system located in the Marina di Ragusa harbor
207 (**Figure 2c**) which is owned by the CNR-IAS (Consiglio Nazionale delle Ricerche - Istituto
208 per lo Studio degli Impatti Antropici e Sostenibilità in Ambiente Marino). This HF radar is part
209 of the CALYPSO HF network operating in the Malta-Sicily channel since 2013. The network
210 is nowadays composed of seven HF Codar SeaSonde systems transmitting at 13.5 MHz (central
211 frequency). The network provides sea surface current maps at 3 km of spatial resolution at
212 hourly scale (Capodici et al., 2019). Each HF radar provides sea state variables (SWH-HF,
213 wave period, wave direction) every 15 minutes; these data are referred to 10 independent
214 annular rings 3 km wide, centered at the HF site location. Data used in this work regard the last
215 annular ring (30 km far from the HF site) showing the best temporal continuity of the
216 measurements. The sea state derived by the HF technology has been deeply validated by several
217 authors (e.g. Long et al., 2011; Lorente et al., 2021; Orasi et al., 2019; Saviano et al., 2019).

218 **3.2.4. Satellite data**

219 The passage of the Helios cyclone in the study area was tracked by means of the High Rate
220 SEVIRI Level 1.5 Image Data. The Level 1.5 image data represents the geolocated and
221 radiometrically pre-processed images that are prepared for subsequent processing steps, e.g.



222 the extraction of meteorological products helpful in our case study. For further information
223 about this methodology you can see the EUMETSAT website
224 (<https://navigator.eumetsat.int/product/EO:EUM:DAT:MSG:HRSEVIRI> last access
225 25/05/2023). In particular, an image at 10.8 μm each 15' was downloaded and analyzed.

226 The above mentioned measures allowed describing the spatial and temporal characteristics of
227 the sea state during the Helios event, that were compared to the features of the microseism.

228 3.3. Spectral Analysis of Microseism

229 The seismic data were corrected for the instrument response and thereafter spectral and
230 amplitude analyses were performed. For the spectral analysis, hourly spectra of the seismic
231 signal were calculated by applying Welch's method (Welch, 1967) with time windows of 81.92
232 s. The hourly spectra, thus obtained, were gathered and represented as spectrograms, with time
233 on the x-axis, frequency on the y-axis, and the \log_{10} of the PSD indicated by a color scale.
234 Some spectrograms obtained from the vertical component of 4 stations are shown in **Figure 3**.
235 Concerning the amplitude, we estimated hourly RMS amplitude time series for the typical
236 microseism frequency bands: 0.2-0.4 Hz (SPSM, **Supplementary Figure 1**), 0.1-0.2 Hz (SM,
237 **Figure 3**) and 0.05-0.07 Hz (PM, **Supplementary Figure 2**).

238 In addition, to show the spatial and temporal distribution of the RMS amplitude during the
239 period under investigation, we plotted the mean RMS amplitude computed on non-overlapped
240 1-day-long moving windows for the three microseism bands. **Each dot, in Figure 4, represents**
241 **a seismic station and the color of the dot relates to the corresponding RMS amplitude at that**
242 **location, as specified in the color bar.** Noteworthy, the colorbar of the PM band
243 (**Supplementary Figure 3**) shows a different range of RMS amplitude highlighting a different
244 response between the PM and the SM and SPSM bands to the sub-tropical system Helios



245 (Figure 4 and Supplementary Figure 4). Furthermore, in this case, we compared the RMS
246 amplitude with the SWH, represented by the contour lines.

247 3.4. Tracking Helios position by Microseism

248 Following Borzi et al. (2022), we used two different and complementary methods to track the
249 position of the sub-tropical system Helios from a seismic point of view. In particular, we use
250 i) a grid search method based on the seismic amplitude decay and ii) array analysis. These
251 methods allow us to track the evolution over time of the location of the centroid of the seismic
252 sources generated by the sea state variations induced by the cyclone. Such seismic data were
253 compared with the cyclone trajectory which was identified by processing the High Rate MSG
254 SEVIRI images. This latter task was accomplished by visually identifying the positions of the
255 cyclone's eye which was clearly identifiable only between 01:00 and 23:00 of the 10 February
256 2023.

257 3.4.1. Grid search method

258 We used the seismic signals recorded by 105 seismic stations (Figure 2a) to map out the
259 position of Helios during the analyzed period by employing a grid search approach (Figure 5).
260 The region, where we executed the grid search, is a bi-dimensional area of 1760 km x 2400 km
261 (minimum longitude: 5°; maximum longitude: 30°; minimum latitude: 30°; maximum latitude:
262 46°) with a spacing of 1°. As shown by several authors who used seismic amplitude decay
263 methods, both to locate microseism sources (Borzi et al. 2022) and seismo-volcanic sources
264 (Battaglia and Aki, 2003; Cannata et al., 2013; Kumagai et al., 2011), the grid spacing is chosen
265 as a compromise between good spatial resolution and reasonable computation time. The
266 microseism source is localized based on the goodness of the linear regression fit (hereafter
267 referred to as R^2) computed for each node of the bi-dimensional (2D) grid previously
268 mentioned. Specifically, the source was identified at the centroid position of all the grid nodes



269 where the R^2 values deviate by no more than 1% from the maximum R^2 value. In this method,
270 we used an RMS signal window of 4 hours and thus we were able to obtain 1 localization every
271 4 hours. In addition, following Borzi et al. (2022), we applied a method to evaluate the
272 statistical significance of the retrieved maximum R^2 value and to test the confidence of the
273 location results. Specifically, we conducted 20 iterations by randomly rearranging the RMS
274 amplitude values among the stations. Then, we calculated the 95th percentile and we obtained
275 a value of 0.27. In accordance with this result, we consider reliable the localizations with R^2
276 values greater than 0.27.

277 It must be underlined that the grid search method used in this study shows various limits that
278 in specific cases can invalidate the source locations. In particular, the first limit concerns the
279 fact that in this method we consider the microseism source as a point-like source, while the
280 microseism is produced in a wide area of the Mediterranean Sea. In this scenario, the
281 localization of the point-like source is determined as the barycentric point of the extended
282 source. However, it is important to consider a limitation of this method related to the presence
283 of multiple sources with similar amplitude in the same frequency range. In such cases, the
284 constrained source location shifts towards a position between the actual seismic source
285 locations (Battaglia et al., 2005), resulting in a significant decrease in R^2 . In our case, we
286 neglect localization showing R^2 values smaller than 0.27, to avoid unreliable localization.

287 **3.4.2. Array analysis**

288 In order to track the location of the sub-tropical system Helios using array techniques, we
289 considered fifteen stations belonging to the Mt. Etna seismic permanent network and used them
290 as a roughly circular array (**Figure 2b**).

291 The Array Response function (ARF) is a good tool to plan the array geometry required to
292 investigate microseism signals or, in this case, to evaluate the performance of a pre-existing



293 array in microseism studies. The ARF, previously obtained by Borzì et al. (2022), exhibits that
294 the roughly circular array has a good response for the PM and SM cases.

295 In this study, we employed the f-k (frequency-wavenumber) analysis technique on microseism
296 signals (e.g. Rost and Thomas, 2002). This approach involves a spectral domain beamforming
297 method that utilizes a grid search of slowness to determine the back azimuth and apparent
298 velocity values that maximize the amplitude of the combined array traces. The result of the f-
299 k analysis is the PSD as a function of slowness. In accordance with Borzì et al. (2022), we
300 followed the subsequent processing steps to implement array analysis on microseismic data:
301 (i) demeaning and detrending; (ii) applying a specific frequency band filter for microseism;
302 (iii) segmenting the data into tapered windows of 120 seconds each; (iv) excluding windows
303 containing seismo-volcanic amplitude transients (such as volcano-tectonic earthquakes, long-
304 period events, and very long-period events) identified using the STA/LTA technique (e.g.,
305 Trnkoczy, 2012); (v) performing f-k analysis for each window by conducting a slowness grid
306 search (ranging from -1 to 1 s/km in the east and north components of the slowness vector)
307 with a spacing of 0.05 s/km. An illustrative example of the outcomes is presented in Figure 5.
308 For further details about these two methods used in this work, you can see Borzì et al. (2022).

309 **3.5. Seismic signature of the Medicanes**

310 In a way to obtain the seismic signature and the main spectral characteristics of the sub-tropical
311 system Helios, we use a method developed by Soubestre et al. (2018). This method was initially
312 developed as a network-based method to detect and classify seismo-volcanic tremors. The
313 proposed method utilizes the coherence of tremor signals within the network, which is
314 determined based on the array covariance matrix. Using this technique, as explained by
315 Soubestre et al. (2018), it is possible to highlight both volcanic tremors and other types of
316 seismic sources such as tectonic earthquakes (local, regional, and teleseismic), and oceanic



317 seismic noise (microseism). This method allows the identification of the spatially coherent
318 individual noise source within a specific network, identified as small spectral width, as opposed
319 to other noises such as local effects that would generate multiple individual sources. For further
320 details about the method, see Soubestre et al. (2018).

321 In this study, we are interested in detecting the microseism produced by the sub-tropical system
322 Helios. Since we are interested in such a microseism, we filtered the signal in the band 0.1-1
323 Hz and resample it to 25 Hz in a way to reduce the computation time. To compute the
324 covariance matrix we use only the vertical component of the seismic signal and a window
325 length of 60 seconds. The analyses were performed using the data recorded by a station set
326 comprising both stations installed near the south Sicilian coast (CLTA and IWAV5) and in the
327 Malta (MSDA) and Linosa (LINA) islands in order to have the microseism source within the
328 selected station set.

329

330 **4. Results and Discussion**

331 We analyze the sea state, derived by four independent techniques, and the seismic data recorded
332 by the i) 105 seismic stations represented in **Figure 2a** and by ii) the 15 Etnean seismic stations
333 (Figure 2b) during the period 8-13 February 2023. We chose a period longer than the real
334 lifetime of the sub-tropical system Helios in a way to include the development, the climax in
335 terms of meteorological events that occurred during the days 9-10 February, and the following
336 loss of intensity.

337 **4.1. Sea state**

338 In **Figure 6**, we show the SWH, the mean wave period and the direction time series recorded
339 during the period 8-13 February 2023 by the buoy of Mazara del Vallo (**Figure 6b, d and f**)
340 and the HF radar installed in Marina di Ragusa harbor (**Figure 6a, c and e**).



341 The buoy data indicates that the sea storm reached its maximum significant wave height of 3.1
342 m at 20:00 on 9 February, with a mean direction of 140° indicating that waves were generated
343 by Scirocco wind, which is the main wave direction for the period under investigation and a
344 period that varies from 5 to 9 s. The data from HF Radar, installed closer to the cyclone position
345 than the buoy, show a maximum SWH of about 6 m recorded on 9 February at 22:30, the mean
346 wave direction was of 100° approximately and the period varies in the range of 5-12 s. Both
347 datasets allowed defining the time interval of the wave storm which spanned between 8-13
348 February 2023. The higher SWH measured by the HF radar agrees with the shorter distance
349 from the cyclone eye (~ 90 km) of this instrument compared to that of the wave buoy (~ 190
350 km).

351 The spatio-temporal distribution of the SWH in the whole area is shown by the hindcast maps
352 in **Figure 7**. Noticeably that the stronger effect of the sub-tropical system Helios on the sea
353 state of the Malta-Sicily channel was the increase of the SWH during 9 - 10 February. On 9
354 February the higher SWH values were recorded mainly in the patch of the sea at the east of
355 Sicily Island and of the Maltese archipelago, whereas the wave storm invaded the whole Malta-
356 Sicily channel on 10 February. Finally, on 11 February the wave storm started moving to the
357 south, reaching the northern part of the African coasts.

358 The comparison between SWH-Hind and SWH-HF revealed a good agreement ($R^2 \sim 0.85$) even
359 if an underestimation of the event by the CMS model (slope of ~ 0.7) was observed
360 (**Supplementary Figure 5**).

361 **4.2. Spectral Analysis and RMS spatial distribution**

362 To perform the spectral analysis we used the 105 seismic stations installed along the Italian,
363 Greek and Maltese coastal areas. In **Figure 3**, we plot the spectrograms and the RMS amplitude
364 time series, obtained by analyzing the vertical component of the seismic signals recorded by
365 four stations installed in Malta (MSDA **Figure 3a**), on Linosa Island (LINA **Figure 3b**), near



366 Pozzallo (IWAV5 **Figure 3c**) and in Central Italy (CELB **Figure 3d**). We chose these four
367 stations to compare the results obtained from the stations installed near the sub-tropical system
368 (LINA, MSDA and IWAV5), with the result obtained from the far station (CELB).

369 As shown by Borzì et al. (2022), in the spectrograms a great part of the energy is focused in
370 the 0.1-1 Hz band, corresponding with the SM and SPSM bands. In addition, it is also evident
371 how the considered stations show a different behavior, in terms of both spectrograms (**Figure**
372 **3**) and RMS amplitude time series (**Figure 3** and **Supplementary Figures 1** and **2**), that
373 depended on their position. In particular, spectrograms and RMS amplitude time series
374 obtained from the data recorded by MSDA (**Figure 3a** and **Supplementary Figure 1a** and **2a**),
375 LINA (**Figure 3b** and **Supplementary Figures 1b** and **2b**) and IWAV5 (**Figure 3c** and
376 **Supplementary Figures 1c** and **2c**) stations, installed close to Helios (**Figure 1** and **Figure**
377 **2**), show the maximum PSD and RMS amplitude values during the time interval 9-11 February
378 2023, highlighted by the vertical dashed lines in **Figure 3**. On the other hand, the spectrogram
379 and RMS amplitude time series of the station CELB (**Figure 3d** and **Supplementary Figures**
380 **1d** and **2d**), installed in the Tyrrhenian area, exhibited the maximum PSD and RMS amplitude
381 values a few days before Helios at the same time as a local storm surge.

382 To show the space-time distribution of the RMS amplitude, we calculate the daily RMS average
383 for the three main microseism bands (PM and SPSM in **Supplementary Figures 3** and **4**, SM
384 in **Figure 4**) during the period 8-13 February 2023. All the three analyzed microseism bands
385 show a relationship with the position of Helios indicated by the five-pointed red star (**Figure**
386 **4c** and **Supplementary Figures 3c** and **4c**). In particular, on 10 February 2023, when Helios
387 reached its climax, the maps in **Figure 4c** (SM) and **Supplementary Figures 3c** and **4c** (PM
388 and SPSM respectively) show a cluster of high RMS values for the stations installed near the
389 sub-tropical system Helios, highlighting a good match between the SM, SPSM, PM and Helios
390 positions.



391 Comparing the results obtained for the sub-tropical system Helios with the results obtained for
392 the Medicane Apollo (Borzi et al., 2022), we observe a similar trend for the SM and SPSM
393 bands and a different behavior for the PM band. In particular, during the Medicane Apollo, the
394 analysis did not show a significant amplitude increase in the PM band, while during the sub-
395 tropical system Helios, the RMS amplitude time series for the PM (Supplementary Figure 2),
396 although with two orders of magnitude smaller, showed a trend similar to the SM (Figure 3)
397 and SPSM (Supplementary Figure 1) ones. Also the space-time distribution shows a good
398 match between the PM (Supplementary Figure 3) and Helios position (Figure 1, 4c and
399 Supplementary Figures 3c and 4c), even if for this band there are stations installed in central
400 Italy that show high RMS amplitude values related to a very local storm surge that occurred at
401 the same time as Helios.

402 The involvement of the PM band in the case of the sub-tropical system Helios can be explained
403 by considering the position of this low-pressure system (Figure 1) and comparing it with the
404 Apollo position. Indeed, the Medicane Apollo develops and moves in the Ionian Sea (Figure
405 2) in an area with a sea depth greater than 2000 m, while the sub-tropical system Helios
406 develops and moves largely in the Sicily Channel, a shallower sea with a depth that reaches a
407 maximum depth of 500 m b.s.l. and an average depth of 316 m b.s.l. In addition, the average
408 depth between Sicily and Malta is about 65 m b.s.l. As outlined in the literature (Bromirski et
409 al., 2005), the production of the PM is hindered in large water depths due to the attenuation of
410 pressure fluctuations, which generate the signal, as a result of depth-dependent amplitude
411 decay. More specifically, the PM is generated solely in depths less than half of the wavelength
412 (where λ represents the wavelength of the oceanic waves generating the pressure fluctuations).

413 If we consider, for the Catania and Mazara areas, a mean waves period of 6.1 and 5.6 s and a
414 peak waves period of 9.7 and 9 s respectively (Agenzia per la Protezione dell’Ambiente e per
415 i Servizi Tecnici Dipartimento Tutela Acque Interne e Marine Servizio Mareografico - Atlante



416 delle onde nei mari italiani), by utilizing the correlation that connects period and wavelength
417 ($\lambda = gT^2/2\pi$ with g acceleration of gravity that is 9.8 m/s^2 and T the period of the waves;
418 Sarpkaya and Isaacson, 1981) we obtain a wavelength, for this part of the Mediterranean sea,
419 ranging between $\sim 45 \text{ m}$ and $\sim 150 \text{ m}$. Considering these wavelengths, the shallow depth of the
420 Sicily Channel, especially in the Malta Channel where the average depth is about 65 m b.s.l. ,
421 and the fact that the generation of the PM occurs only for depths less than $\frac{1}{2} \lambda$ (Bromirski et
422 al., 2005), we can remark that the generation of the PM is possible in the Sicily Channel, while
423 can not occur in the Ionian Sea except in limited areas near the coastline. This is evident in our
424 analysis, and in particular in the RMS amplitude time series. Indeed in the sub-tropical system
425 Helios case, which occurred in the Sicily Channel, we can note a similar trend between the
426 three analyzed microseism bands (**Figure 3** and **Supplementary Figures 1 and 2**), while in the
427 case of the Mediane Apollo, that developed in the Ionian Sea (Borzì et al., 2022), we observe
428 an RMS amplitude increase only for the SM and SPSM bands and no significant variations in
429 the PM bands.

430 **4.3. Comparing the RMS amplitude with the SWH**

431 As mentioned before, microseism is a continuous seismic signal linked to the hydrosphere-
432 solid Earth energy transfer and, as demonstrated by several authors (e.g. Arduin et al., 2012;
433 Bromirski et al., 1999; Bromirski et al., 2005; Cutroneo et al., 2021; Ferretti et al., 2013, 2018),
434 the amplitude of this signal is strictly related to the sea state and in particular to the SWH. To
435 analyze the relationship between microseism and SWH, we plot in **Figure 8a** the RMS
436 amplitude time series for the station IWAV5 and the SWH time series derived from both HF
437 Radar (SWH-HF) and hindcast maps (SWH-Hind) (the position of IWAV5 and HF radar are
438 respectively shown in **Figure 2a** and **2c**). The sea state information provided by the Mazara del
439 Vallo buoy was not taken into account in this analysis because of the long distance between
440 this instrument and the cyclone eye. We chose station IWAV5 because it is one of the nearest



441 stations to the cyclone eye. Also, as it is possible to see in **Figure 3a, b and c**, all the seismic
442 stations installed in the Sicily Channel area show very similar microseism amplitude patterns.
443 The time series of SWH-Hind was obtained by computing the median value of the SWH data
444 within a wide area of the Sicily Channel shown in **Figure 8d**. In general, the three datasets
445 exhibit a good agreement among them. In particular, we observe an increase that occurs almost
446 simultaneously for SWH-HF, SWH-Hind and the RMS amplitude. However, from the first
447 hours of 10 February, the SWH-HF started showing a different behavior compared to SWH-
448 Hind; indeed, the SWH-HF decreased while the SWH-Hind continued to show high values up
449 to the end of 10 February. This difference can be explained by considering that the HF Radar
450 provides information about the SWH for a limited area while SWH-Hind gives median
451 information about a wide area of the Sicily Channel. It is interesting to note that the microseism
452 amplitude follows more closely the areal sea state, shown by the SWH-Hind series, than the
453 punctual one, shown by the SWH-HF. We can note this in both a qualitative way in the time
454 series of **Figure 8a** and a quantitative way in the cross-plots of **Figures 8b and c**. For both the
455 cross-plots we calculated the R^2 value, to evaluate the goodness of the linear regression, and
456 we obtain R^2 values equal to 0.68 and 0.85, for the cross-plot RMS amplitude vs SWH-HF and
457 RMS amplitude vs SWH-Hind, respectively. The higher value of R^2 for the RMS amplitude -
458 SWH-Hind relationship can be explained by considering that microseism recorded by a seismic
459 station is generated by multiple extended sources distributed on a wide portion of the sea.

460 **4.4. Localization analysis**

461 As concerns the microseism source location, we performed the location analysis for the PM,
462 SM and SPSM using both the array techniques and the grid search method based on the seismic
463 amplitude decay. Concerning the array techniques, we chose to focus on the SM band since,
464 according to the information from the ARF, we expect reliable localizations only on the PM
465 and SM bands, while for the SPSM band appears spatial aliasing. As for the grid search method,



466 we obtained reliable locations only for the SM and SPSM bands, while for the PM band,
467 although we got localizations in agreement with the cyclone position, the associated R^2 values
468 turned out to be slightly lower than the threshold from which we can consider the locations
469 reliable.

470 By the grid search method, we obtained reliable locations from 9 February 2023 at 8:00 to 11
471 February 2023 at 00:00 (**Supplementary Figure 6**). In agreement with satellite images (**Figure**
472 **1**), on 9 February 2023, the sub-tropical system Helios was not yet well-developed and did not
473 show the cyclone eye. Indeed, during this day, we are able to locate a storm surge, probably
474 linked to the primitive formation of Helios, that occurred in the Ionian Sea. In particular, our
475 localizations, on 9 February from 8:00 to 20:00, indicate the source position near to the south-
476 eastern part of Sicily in agreement with the hindcast data showing for this area SWH greater
477 than 5 meters (**Figure 4b and 7**). During the following hours, our localizations
478 (**Supplementary Figure 6**) show a small but continuous shift of the source toward the Malta
479 area (**Figure 5**), in agreement with the relatively stable position of the cyclone eye for the first
480 hours of 10 February 2023, retrieved from SEVIRI data (**Figure 1**). Successively, the sub-
481 tropical system rapidly loses its strength and runs out completely on the day of 11 February
482 2023, making landfall against the Libyan coast. In **Table 1** we summarised the main features
483 of the microseism source located by using the grid search method during the days 9-10
484 February 2023 and compared these with the results obtained during the period 01:00 - 23:00 of
485 10 February 2023 in terms of the coordinates of the cyclone eye retrieved by SEVIRI data.
486 During the first hours of the cyclone life, the coordinates of the cyclone eye and the microseism
487 source show only a small offset that, as explained in section 3.4.1, can be due to the fact that
488 the point-like microseism source corresponds with the barycentric position of an extended
489 source and it is expected that the microseism source location could differ from the cyclone eye.
490 During the following hours, as shown in **Figure 1**, the cyclone moved southward until the time



491 when the cyclone made landfall against the Libyan coast. This shift is not visible in the
492 microseism location results, probably due to the lack of seismic stations in Africa, that would
493 help locate more accurately seismic sources placed close to the African Coastlines. In
494 **Supplementary Figure 7** we plot the temporal distribution of the R^2 values and compare this
495 with the SWH-Hind time series. These two datasets show a good agreement and highlight that
496 the higher R^2 values obtained from the grid search method are influenced by the presence of
497 the sub-tropical system Helios.

498 Concerning the array analysis, the result obtained for the PM band shows that, for the period
499 9-11 February, the back azimuth values pointed toward the Ionian Sea (**Supplementary Figure**
500 **8**) with apparent velocity values of ~ 3.0 km/s (**Supplementary Figure 9**). For the same days,
501 the back azimuth values for the SM band pointed toward the same region (**Supplementary**
502 **Figure 10**), with apparent velocity values of ~ 2.0 km/s (**Supplementary Figure 11**).

503 For the PM and the SPSM bands, we obtained reliable locations only by one of the two used
504 methods (array technique for the PM and grid search method for the SPSM), while for the SM
505 we obtained reliable locations from both the aforementioned methods and we can compare the
506 results obtained independently from these two methods. We can observe that the grid search
507 method based on the seismic amplitude decay is able to detect both the storm surge that
508 occurred in the Ionian sea and the following formation of the sub-tropical system Helios
509 (**Supplementary Figure 6**), and in particular by this method, we localize the cyclone as a
510 point-like source, considered as a barycentre of an extended source. The array technique
511 instead provides back azimuth values pointing toward the Ionian Sea for the entire period of 9-
512 11 February (**Supplementary Figure 10**). From these results, we can note that the two methods
513 are influenced by different sources. This different result can be explained based on the spatial
514 station distribution. Indeed, if we consider the grid search method we use a wide station
515 network including stations installed near the sub-tropical system Helios (MSDA, CLTA,



516 IWAV5, LINA and other stations), while the Etnean array includes 15 stations clustered in a
517 small area. In addition, the distance array center-Ionian Sea (~20 km) is smaller than the
518 distance array center-Sicily Channel (~90 km). During the period taken into account, we have
519 the coexistence of two strength sources, the first in the Ionian Sea (storm surge with SWH
520 greater than 5 m) and the other, probably the strongest, in the Sicily Channel (Helios), both
521 represented by the red contour line in **Figure 4c**. Hence, the coexistence of two sources and
522 the great difference in distance between the array center and the Ionian Sea and the array center
523 and the Sicily channel does not allow us to locate the sub-tropical system Helios with the array
524 technique, which gives us back azimuth values pointing always toward the nearest source.

525 **4.5. Seismic signature**

526 To show the main spectral characteristics of the sub-tropical system Helios, we used the method
527 developed by Soubestre et al. (2018). From our analysis, the evolution in time of the
528 microseism spectral characteristics between the first 24 hours and the following ones is evident
529 (**Figure 9**). In particular, with the vertical dashed lines in **Figure 9**, we show the time interval
530 when Helios develops, reaches the climax and loses power to run out. The first 24 hours are
531 characterized by the lack of a clear predominance of a particular frequency range. Starting from
532 early 9 February 2023 (first vertical white dashed line), we can observe high coherence values
533 clustered on a narrow frequency range between about 0.14 and 0.25 Hz, and this frequency
534 range is constant until the 80 hours (vertical black dashed line) corresponding to the morning
535 of 11 February. Successively, the frequency with the highest coherence starts to increase
536 reaching a value of about 0.35 Hz before the exhaustion of the phenomenon. This increase in
537 the frequency could be related to the landfall of Helios against the Lybian coast
538 (<https://twitter.com/medcyclones/status/1624143740800536591?s=20>, last access 23/05/2023
539). Indeed, as described in the literature (Gerstof et al., 2006; Lin et al., 2017; Sun et al., 2013),
540 there exists a relationship between the frequency, the sea depth and the development of local



541 wave motion near the coastline. In particular, Gerstof et al. (2006) show an increase in the
542 microseism frequency during the two landfalls of Hurricane Katrina. Similar results are shown
543 by Sun et al. (2013), who highlighted an increase in the intensity of the microseism for the SM
544 and SPSM and the frequency increase from the SM band toward the SPSM one during the
545 approaching of the three analyzed typhoons against the Chinese coast. Finally, Lin et al. (2017)
546 show an increase in the microseism frequency during the first landfall of typhoon Megi.
547 Similarly, we obtained an increase in frequency during the time interval when Helios
548 approached the Lybian coastline and made landfall on 11 February
549 (<https://twitter.com/medcyclones/status/1624143740800536591?s=20>, last access
550 23/05/2023). We were also able to observe the gradual loss of power of the sub-tropical system
551 highlighted by ever-lower coherence values until its disappearance.

552 **5. Conclusions**

553 Several works have dealt with the relationship between microseism and several meteorological
554 phenomena, considering in particular storm surges (Ardhuin et al., 2019; Cannata et al., 2020;
555 Guerin et al., 2022; Moschella et al., 2020) and different types of cyclones (Borzì et al., 2022;
556 Bromirski, 2001; Bromirski et al., 2005; Gerstoft et al., 2006; Gualtieri et al., 2018; Lin et al.,
557 2017; Retailleau and Gualtieri, 2019, 2021; Zhang et al., 2010) that affect various parts of the
558 world (hurricanes, typhoons, tropical cyclones and medicanes). In this work, we analyzed the
559 relationship between the three main microseism bands (PM, SM and SPSM) and the sub-
560 tropical system Helios that occurred in the Mediterranean Sea during the time interval 9-11
561 February 2023. Although all the meteorological parameters suggest that Helios has not been
562 able to reach the fully Medicane characteristics, remaining a rather weak sub-tropical system,
563 the proximity of this cyclone to the southeastern Sicilian and Maltese coastal area has caused
564 heavy rainfall, strong wind gusts and violent storm surge in the two above mentioned areas.



565 To obtain information about the sea state we take into account the data of hindcast maps,
566 wavemeter buoy, HF radar and SEVIRI images. The first three methodologies show an increase
567 in the SWH during the period under investigation, with a climax during the days 9-10 February
568 2023, due to the presence of the sub-tropical system Helios. **In particular, the HF radar and the**
569 **hindcast maps exhibit an SWH of about 6 meters while the wavemeter buoy shows an SWH of**
570 **about 3 meters.** This difference is only linked to the position where the two instruments are
571 installed, indeed the HF radar is installed at about 90 km from the cyclone eye while the
572 wavemeter buoy is installed at about 190 km. SEVIRI images provide information about the
573 location of the cyclone eye that is clearly visible between 01:00 and 23:00 on 10 February
574 2023.

575 To analyze this meteorological phenomenon from a seismic point of view, we selected 120
576 seismic stations installed along the Italian, Maltese and Greek coastal areas: i) 105 used in
577 spectral and amplitude analysis, in the grid search method and 4 of these to obtain the seismic
578 signature of Helios using the method of the covariance matrix; ii) 15 in array analysis. The
579 results, obtained from the spectral analysis, highlight that the seismic signals, in particular the
580 PM, SM and SPSM bands, are affected by the storm surge and by the sub-tropical system
581 Helios. This is evident considering the RMS amplitude time series, the spectrograms and the
582 RMS amplitude space-time distribution, in which it is possible to observe that the amplitude of
583 the microseism signal, in the three main bands above mentioned, shows a similar trend and it
584 is greater during the period 9-10 February 2023 for the stations installed close to the Sicily
585 Channel (for example the stations MSDA, LINA and IWAV5), while the stations installed
586 farther from Helios (for example CELB) show a different behavior conditioned by local
587 sources. Furthermore, the increase of the RMS amplitude for the PM band can be explained on
588 the basis of the position where Helios develops. Indeed, as explained in the literature
589 (Bromirski et al., 2005), the generation of the PM is limited in the areas where the depth of the



590 sea bottom is smaller than $\frac{1}{2}\lambda$ (where λ is the wavelength of the sea waves) as a consequence
591 of the amplitude decay of the pressure fluctuations. The Sicily Channel and in particular the
592 area between Malta and Sicily (Malta Channel), where Helios stood still for the entire 10
593 February 2023, shows an average depth of about 65 m b.s.l., and considering wavelength
594 between ~ 45 m and ~ 150 m it is possible the generation of the PM for this area.

595 By comparing the SWH recorded by HF Radar, SWH retrieved by hindcast data and the RMS
596 amplitude recorded at the station IWAV5, we observe that the RMS amplitude time series
597 shows a trend more similar to that of hindcast data than to the HF Radar data. This could be
598 explained by considering that the microseism is a seismic signal generated by multiple and
599 extended sources in a large area of the sea and hence its amplitude is related to the state of a
600 wide portion of the sea.

601 We used two different methods to track the position of the sub-tropical system Helios during
602 its lifetime and, through the performed analysis, we were able to locate both the storm surge
603 that occurred in the Ionian Sea and Helios. In particular, using the grid search method based on
604 the seismic amplitude decay we located the storm surge in the Ionian Sea on 9 February 2023
605 and the sub-tropical system Helios on the next day, while with the array technique, we located
606 only the storm surge in the Ionian Sea as a consequence of the position of the array closer to
607 the Ionian Sea than to the Sicily Channel. The location obtained both for the storm surge and
608 for the sub-tropical system Helios, during the first hours of its life, is in agreement with the real
609 position of the two meteorological phenomena shown by the hindcast maps and satellite
610 images. Successively, the sub-topical system Helios moved southward until the time when the
611 cyclone made landfall against the Libyan coast while the microseism source continued to show
612 a stable position near Malta Island. This difference between the two positions is probably due
613 to the lack of seismic stations in Africa, that does not locate accurately microseism sources
614 placed close to the African Coastlines. In addition, using the method of the covariance matrix,



615 we obtained the seismic signature of the sub-tropical system Helios. In particular, during the
616 development and climax of the cyclone Helios, we can observe high coherence values clustered
617 on a narrow frequency range between about 0.14 and 0.25 Hz that, as described in the literature,
618 corresponds to the microseism bands (SM and SPSM) most affected by cyclonic activity. This
619 narrow frequency range stays constant until the time when Helios makes landfall when we
620 observe an increase in the frequency until a value of about 0.35 Hz probably linked to the
621 decrease of the sea depth and the development of local wave motion near the coastline.

622 Starting from Borzì et al. (2022), this work aims at studying and monitoring the Mediterranean
623 cyclones through microseism and its integration with sea state data. It underlines that it is
624 possible to extract information about these meteorological phenomena by an innovative system
625 for the sea state monitoring that includes not only the classical instruments (such as wavemeter
626 buoys, radar HF and geostationary satellites) but also seismometers. In particular, the large
627 number of broadband seismic stations, installed for earthquake and volcanic monitoring, can
628 compensate for the lack of data of the classical instruments mentioned above, more often
629 affected by instrument breakage.

630 Finally, since we obtained the seismic signature of this particular Mediterranean cyclone we
631 can compare it with the seismic signature of other Mediterranean events (Medicane and
632 common storms) to identify the similarities and differences in the spectral content of different
633 Mediterranean cyclones and other more common events. The characterization of the seismic
634 signature of these events could be useful to identify Mediterranean cyclones by old
635 seismograms, and hence to reconstruct the temporal variability (in terms of occurrence rate and
636 intensity) of these extreme meteo-marine events whose evolution seems to be strictly linked to
637 the global warming (e.g. Emanuel, 2005; Reguero et al., 2019).

638

639



640 **Data availability**

641 The seismic data, in the miniseed format used in this study, can be downloaded through the
642 ORFEUS-EIDA database (<http://www.orfeus-eu.org/data/eida/>). All the seismic stations used
643 in this study, along with their main features, are reported in Supplementary Tables 1 and 2. The
644 hindcast data are available online on the Copernicus site
645 (<https://resources.marine.copernicus.eu/products>). The Italian buoy data (Mazara del Vallo) are
646 available on the ISPRA website (<https://dati.isprambiente.it/>) and on the MAREOGRAFICO
647 website (www.mareografico.it). Satellite data are available on the EUMETSAT website
648 (<https://navigator.eumetsat.int/product/EO:EUM:DAT:MSG:HRSEVIRI>). The HF Radar data
649 are available on the CALYPSO project website by compiling the form indicated on the web
650 page (https://www.calypsosouth.eu/index.php/welcome/open_page/50/0) or by contacting
651 giuseppe.ciraolo@unipa.it or salvatore.aronica@cnr.it.

652 **Acknowledgments**

653 The authors thank the i-waveNET “Implementation of an innovative system for monitoring the
654 state of the sea in climate change scenarios” project, funded by the Interreg Italia-Malta
655 Programme (<https://iwavenet.eu/>; notice 2/2019 Axis 3; project code C2-3.2-106). A.M.B.
656 thanks the PON “Ricerca e Innovazione 2014-2020 Azione IV.5 - Dottorati su tematiche
657 green”. The authors are grateful to Prof. Vittorio Scribano, the Museo Archeologico di
658 Kamarina, Parco di Kamarina e Cava D'Ispica - Direttore Arch. Domenico Buzzone and the
659 Centro Polifunzionale di Protezione Civile - Dott.ssa Emilia Pluchinotta, for hosting the
660 seismic stations installed in the framework of the i-waveNET project and used in this work
661 (IWAV2, IWAV3, IWAV3). This study has been conducted using E.U. Copernicus Marine
662 Service Information, https://doi.org/10.25423/cmcc/medsea_multiyear_wav_006_012. The
663 seismic data, downloaded using the EIDA and ORFEUS webservices, belong to the AC, FR,



664 HC, HL, HP, IV, ML and MN networks. T.L. and R.D.P. thank the research project
665 “SEISMOSTORM” funded by the BRAIN-be 2 program of the Federal Science Policy
666 (BELSPO).

667

668

669 **References**

670

671 ● Agenzia per la Protezione dell’Ambiente e per i Servizi Tecnici Dipartimento Tutela
672 Acque Interne e Marine Servizio Mareografico - Atlante delle onde nei mari italiani -
673 Università degli studi di Roma Tre
674 [http://opac.apat.it/sebina/repository/catalogazione/immagini/pdf/atlante%20mari%201](http://opac.apat.it/sebina/repository/catalogazione/immagini/pdf/atlante%20mari%20160_2_.pdf)
675 [_60_2_.pdf](http://opac.apat.it/sebina/repository/catalogazione/immagini/pdf/atlante%20mari%20160_2_.pdf)

676 ● Androulidakis, Y., Makris, C., Mallios, Z., Pytharoulis, I., Baltikas, V., & Krestenitis,
677 Y. Storm surges during a Mediane in the Ionian Sea. *Proceedings of the Marine and*
678 *Inland Waters Research Symposium, Porto Heli, Greece.* p. 16-19, 2022..

679 ● Ardhuin, F., & Roland, A. "Coastal wave reflection, directional spread, and
680 seismoacoustic noise sources." *Journal of Geophysical Research: Oceans* 117.C11,
681 2012.

682 ● Ardhuin, F.; Gualtieri, L.; Stutzmann, E. How ocean waves rock the Earth: Two
683 mechanisms explain microseisms with periods 3 to 300 s. *Geophysical Research*
684 *Letters*, 42.3: 765-772, <https://doi.org/10.1002/2014GL062782>, 2015.

685 ● Ardhuin, F., Stopa, J. E., Chapron, B., Collard, F., Husson, R., Jensen, R. E., ... &
686 Young, I. Observing sea states. *Frontiers in Marine Science*, 124,
687 <https://doi.org/10.3389/fmars.2019.00124>, 2019.



- 688 • Battaglia, J., & Aki, K. Location of seismic events and eruptive fissures on the Piton de
689 la Fournaise volcano using seismic amplitudes. *Journal of Geophysical Research: Solid*
690 *Earth*, 108(B8), <https://doi.org/10.1029/2002JB002193>, 2003.
- 691 • Battaglia, J., Aki, K., & Ferrazzini, V. Location of tremor sources and estimation of
692 lava output using tremor source amplitude on the Piton de la Fournaise volcano: 1.
693 Location of tremor sources. *Journal of volcanology and geothermal research*, 147(3-4),
694 268-290, <https://doi.org/10.1016/j.jvolgeores.2005.04.005>, 2005.
- 695 • Bencivenga, M., Nardone, G., Ruggiero, F., & Calore, D., The Italian Data Buoy
696 Network. *WTI Trans. Eng. Sci.*, 74, 321–332, 2012.
- 697 • Borzi, A. M., Minio, V., Cannavò, F., Cavallaro, A., D'Amico, S., Gauci, A., ... &
698 Cannata, A. Monitoring extreme meteo-marine events in the Mediterranean area using
699 the microseism (Medicane Apollo case study). *Scientific Reports*, 12(1), 21363,
700 <https://doi.org/10.1038/s41598-022-25395-9>, 2022.
- 701 • Bouin, M. N., & Lebeaupin Brossier, C. Surface processes in the 7 November 2014
702 medicane from air–sea coupled high-resolution numerical modelling. *Atmospheric*
703 *Chemistry and Physics*, 20(11), 6861-6881, 2020.
- 704 • Bromirski, Peter D., Reinhard E. Flick, and Nicholas Graham. "Ocean wave height
705 determined from inland seismometer data: Implications for investigating wave climate
706 changes in the NE Pacific." *Journal of Geophysical Research: Oceans* 104.C9 20753-
707 20766, <https://doi.org/10.1029/1999JC900156>, 1999.
- 708 • Bromirski, Peter D. "Vibrations from the “perfect storm”." *Geochemistry, Geophysics,*
709 *Geosystems* 2.7, <https://doi.org/10.1029/2000GC000119>, 2001.
- 710 • Bromirski, Peter D., Fred K. Duennbier, and Ralph A. Stephen. "Mid-ocean
711 microseisms." *Geochemistry, Geophysics, Geosystems* 6.4,
712 <https://doi.org/10.1029/2004GC000768>, 2005.



- 713 • Cannata, A., Di Grazia, G., Aliotta, M., Cassisi, C., Montalto, P., & Patanè, D.
714 Monitoring seismo-volcanic and infrasonic signals at volcanoes: Mt. Etna case study.
715 *Pure and Applied Geophysics*, 170, 1751-1771, [https://doi.org/10.1007/s00024-012-](https://doi.org/10.1007/s00024-012-0634-x)
716 0634-x, 2013.
- 717 • Cannata, A., Cannavò, F., Moschella, S., Di Grazia, G., Nardone, G., Orasi, A., ... &
718 Gresta, S. Unravelling the relationship between microseisms and spatial distribution of
719 sea wave height by statistical and machine learning approaches. *Remote Sensing*, 12(5),
720 761, <https://doi.org/10.3390/rs12050761>, 2020.
- 721 • Carrió, D. S., Homar, V., Jansa, A., Romero, R., & Picornell, M. A. Tropicalization
722 process of the 7 November 2014 Mediterranean cyclone: Numerical sensitivity study.
723 *Atmospheric Research*, 197, 300-312, <https://doi.org/10.1016/j.atmosres.2017.07.018>,
724 2017.
- 725 • Capodici, F., Cosoli, S., Ciruolo, G., Nasello, C., Maltese, A., Poulain, P. M., ... &
726 Gauci, A. Validation of HF radar sea surface currents in the Malta-Sicily Channel.
727 *Remote sensing of environment*, 225, 65-76, <https://doi.org/10.1016/j.rse.2019.02.026>,
728 2019.
- 729 • Cavicchia, Leone, Hans von Storch, and Silvio Gualdi. "Mediterranean tropical-like
730 cyclones in present and future climate." *Journal of Climate* 27.19, 7493-7501,
731 <https://doi.org/10.1175/JCLI-D-14-00339.1>, 2014.
- 732 • Comellas Prat, A., Federico, S., Torcasio, R. C., D'Adderio, L. P., Dietrich, S., &
733 Panegrossi, G. Evaluation of the sensitivity of medicane Ianos to model microphysics
734 and initial conditions using satellite measurements. *Remote Sensing*, 13(24), 4984,
735 <https://doi.org/10.3390/rs13244984>, 2021.
- 736 • Cutroneo, L., Ferretti, G., Barani, S., Scafidi, D., De Leo, F., Besio, G., & Capello, M..
737 Near real-time monitoring of significant sea wave height through microseism



- 738 recordings: Analysis of an exceptional sea storm event. *Journal of Marine Science and*
739 *Engineering*, 9(3), 319, <https://doi.org/10.3390/jmse9030319>, 2021.
- 740 • Dafis, S., Rysman, J. F., Claud, C., & Flaounas, E. Remote sensing of deep convection
741 within a tropical-like cyclone over the Mediterranean Sea. *Atmospheric Science Letters*,
742 19(6), e823, <https://doi.org/10.1002/asl.823>, 2018.
- 743 • Davies R. Cyclone Helios, Malta and Italy, February 2023,
744 <https://www.efas.eu/en/news/cyclone-helios-malta-and-italy-february-2023>, last
745 access 13/04/2023)
- 746 • Delibera di Giunta - Regione Siciliana
747 ([https://www2.regione.sicilia.it/deliberegiunta/file/giunta/allegati/N.099_15.02.2023.p](https://www2.regione.sicilia.it/deliberegiunta/file/giunta/allegati/N.099_15.02.2023.pdf)
748 [df](https://www2.regione.sicilia.it/deliberegiunta/file/giunta/allegati/N.099_15.02.2023.pdf), last access 13/04/2023)
- 749 • Di Muzio, E., Riemer, M., Fink, A. H., & Maier-Gerber, M. Assessing the predictability
750 of Medicanes in ECMWF ensemble forecasts using an object-based approach.
751 *Quarterly Journal of the Royal Meteorological Society*, 145(720), 1202-1217,
752 <https://doi.org/10.1002/qj.3489>, 2019.
- 753 • Emanuel, K. Increasing destructiveness of tropical cyclones over the past 30 years.
754 *Nature*, 436(7051), 686-688, <https://doi.org/10.1038/nature03906>, 2005.
- 755 • Faranda, D., Bourdin, S., Ginesta, M., Krouma, M., Noyelle, R., Pons, F., ... & Messori,
756 G. A climate-change attribution retrospective of some impactful weather extremes of
757 2021. *Weather and Climate Dynamics*, 3(4), 1311-1340, [https://doi.org/10.5194/wcd-](https://doi.org/10.5194/wcd-3-1311-2022)
758 [3-1311-2022](https://doi.org/10.5194/wcd-3-1311-2022), 2022.
- 759 • Ferretti, G., Zunino, A., Scafidi, D., Barani, S., & Spallarossa, D. On microseisms
760 recorded near the Ligurian coast (Italy) and their relationship with sea wave height.
761 *Geophysical Journal International*, 194(1), 524-533,
762 <https://doi.org/10.1093/gji/ggt114>, 2013.



- 763 • Ferretti, G., Barani, S., Scafidi, D., Capello, M., Cutroneo, L., Vagge, G., & Besio, G.
764 Near real-time monitoring of significant sea wave height through microseism
765 recordings: An application in the Ligurian Sea (Italy). *Ocean & Coastal Management*,
766 165, 185-194, <https://doi.org/10.3390/jmse9030319>, 2018.
- 767 • Flaounas, E., Davolio, S., Raveh-Rubin, S., Pantillon, F., Miglietta, M. M., Gaertner,
768 M. A., ... & Ricard, D. Mediterranean cyclones: Current knowledge and open questions
769 on dynamics, prediction, climatology and impacts. *Weather and Climate Dynamics*,
770 3(1), 173-208, <https://doi.org/10.5194/wcd-3-173-2022>, 2022.
- 771 • Gerstoft, P., Fehler, M. C., & Sabra, K. G. When katrina hit california. *Geophysical*
772 *Research Letters*, 33(17), <https://doi.org/10.1029/2006GL027270>, 2006.
- 773 • Gualtieri, L., Camargo, S. J., Pascale, S., Pons, F. M., & Ekström, G. The persistent
774 signature of tropical cyclones in ambient seismic noise. *Earth and Planetary Science*
775 *Letters*, 484, 287-294, <https://doi.org/10.1016/j.epsl.2017.12.026>, 2018.
- 776 • Guerin, G., Rivet, D., Van Den Ende, M. P. A., Stutzmann, E., Sladen, A., & Ampuero,
777 J. P. Quantifying microseismic noise generation from coastal reflection of gravity
778 waves recorded by seafloor DAS. *Geophysical Journal International*, 231(1), 394-407,
779 <https://doi.org/10.1093/gji/ggac200>, 2022.
- 780 • Hart, R. E. A cyclone phase space derived from thermal wind and thermal asymmetry.
781 *Monthly weather review*, 131(4), 585-616, [https://doi.org/10.1175/1520-0493\(2003\)131%3C0585:ACPSDF%3E2.0.CO;2](https://doi.org/10.1175/1520-0493(2003)131%3C0585:ACPSDF%3E2.0.CO;2), 2003.
- 782 • Hasselmann, Klaus. "A statistical analysis of the generation of microseisms." *Reviews*
783 *of Geophysics* 1.2, 177-210, 1963.
- 784 • Haubrich, Richard A., and Keith McCamy. "Microseisms: Coastal and pelagic
785 sources." *Reviews of Geophysics* 7.3: 539-571, 1969.
- 786



- 787 • Kerkmann J. and Bachmeier S. Development of a tropical storm in the Mediterranean
788 Sea (6–9 November 2011). Available at: [https://www.eumetsat.int/tropical-storm-](https://www.eumetsat.int/tropical-storm-develops-mediterranean-sea)
789 develops-mediterranean-sea (last access: 15 February 2023), 2011.
- 790 • Korres, G., Ravdas, M., & Zacharioudaki, A. Mediterranean Sea Waves Hindcast
791 (CMEMS MED-Waves) [Data set]. Copernicus Monitoring Environment Marine
792 Service (CMEMS).
793 https://doi.org/10.25423/CMCC/MEDSEA_HINDCAST_WAV_006_012, 2019
- 794 • Kumagai, H., Placios, P., Ruiz, M., Yepes, H., & Kozono, T. Ascending seismic source
795 during an explosive eruption at Tungurahua volcano, Ecuador. *Geophysical Research*
796 *Letters*, 38(1), <https://doi.org/10.1029/2010GL045944>, 2011.
- 797 • Lagouvardos, K., Karagiannidis, A., Dafis, S., Kalimeris, A., & Kotroni, V. Ianos—A
798 hurricane in the Mediterranean. *Bulletin of the American Meteorological Society*,
799 103(6), E1621-E1636, <https://doi.org/10.1175/BAMS-D-20-0274.1>, 2022.
- 800 • Lin, J., Lin, J., & Xu, M. Microseisms generated by super typhoon Megi in the western
801 Pacific Ocean. *Journal of Geophysical Research: Oceans*, 122(12), 9518-9529,
802 <https://doi.org/10.1002/2017JC013310>, 2017.
- 803 • Lionello, P., Conte, D., & Reale, M. The effect of cyclones crossing the Mediterranean
804 region on sea level anomalies on the Mediterranean Sea coast. *Natural Hazards and*
805 *Earth System Sciences*, 19(7), 1541-1564, <https://doi.org/10.5194/nhess-19-1541-2019>,
806 2019.
- 807 • Long, R. M., Barrick, D., Largier, J. L., & Garfield, N. Wave observations from central
808 California: SeaSonde systems and in situ wave buoys. *Journal of Sensors*,
809 <https://doi.org/10.1155/2011/728936>, 2011.



- 810 • Longuet-Higgins, Michael Selwyn. "A theory of the origin of microseisms."
811 *Philosophical Transactions of the Royal Society of London. Series A, Mathematical and*
812 *Physical Sciences* 243.857, 1-35, 1950.
- 813 • Lorente, P., Lin-Ye, J., Garcia-Leon, M., Reyes, E., Fernandes, M., Sotillo, M. G., ...
814 & Alvarez-Fanjul, E. On the performance of high frequency radar in the western
815 mediterranean during the record-breaking storm gloria. *Frontiers in Marine Science*, 8,
816 645762, <https://doi.org/10.3389/fmars.2021.645762>, 2021.
- 817 • Miglietta, M. M., Moscatello, A., Conte, D., Mannarini, G., Lacorata, G., & Rotunno,
818 R. Numerical analysis of a Mediterranean ‘hurricane’ over south-eastern Italy:
819 Sensitivity experiments to sea surface temperature. *Atmospheric research*, 101(1-2),
820 412-426, <https://doi.org/10.1016/j.atmosres.2011.04.006>, 2011.
- 821 • Miglietta, M. M., Laviola, S., Malvaldi, A., Conte, D., Levizzani, V., & Price, C.
822 Analysis of tropical-like cyclones over the Mediterranean Sea through a combined
823 modeling and satellite approach. *Geophysical Research Letters*, 40(10), 2400-2405,
824 <https://doi.org/10.1002/grl.50432>, 2013.
- 825 • Miglietta, M. M., & Rotunno, R. Development mechanisms for Mediterranean tropical-
826 like cyclones (medicanes). *Quarterly Journal of the Royal Meteorological Society*,
827 145(721), 1444-1460, <https://doi.org/10.1002/qj.3503>, 2019.
- 828 • Moschella, S., Cannata, A., Cannavò, F., Di Grazia, G., Nardone, G., Orasi, A., ... &
829 Gresta, S. Insights into microseism sources by array and machine learning techniques:
830 Ionian and Tyrrhenian sea case of study. *Frontiers in Earth Science*, 8, 114,
831 <https://doi.org/10.3389/feart.2020.00114>, 2020.
- 832 • Nastos, P. T., Papadimou, K. K., & Matsangouras, I. T. Mediterranean tropical-like
833 cyclones: Impacts and composite daily means and anomalies of synoptic patterns.



- 834 *Atmospheric Research*, 208, 156-166, <https://doi.org/10.1016/j.atmosres.2017.10.023>,
835 2018.
- 836 • Oliver, J., & Page, R. Concurrent storms of long and ultralong period microseisms.
837 *Bulletin of the Seismological Society of America*, 53(1), 15-26, 1963.
- 838 • Orasi, A., Picone, M., Drago, A., Capodici, F., Gauci, A., Nardone, G., ... & Alonso-
839 Martirena, A. HF radar for wind waves measurements in the Malta-Sicily Channel.
840 *Measurement*, 128, 446-454, <https://doi.org/10.1016/j.measurement.2018.06.060>,
841 2018.
- 842 • Pravia-Sarabia, E., Gómez-Navarro, J. J., Jiménez-Guerrero, P., & Montávez, J. P.
843 Influence of sea salt aerosols on the development of Mediterranean tropical-like
844 cyclones. *Atmospheric Chemistry and Physics*, 21(17), 13353-13368,
845 <https://doi.org/10.5194/acp-21-13353-2021>, 2021.
- 846 • Portmann, R., González-Alemán, J. J., Sprenger, M., & Wernli, H. How an uncertain
847 short-wave perturbation on the North Atlantic wave guide affects the forecast of an
848 intense Mediterranean cyclone (Medicane Zorbas). *Weather and Climate Dynamics*,
849 1(2), 597-615, <https://doi.org/10.5194/wcd-1-597-2020>, 2020.
- 850 • Reguero, B. G., Losada, I. J., & Méndez, F. J. A recent increase in global wave power
851 as a consequence of oceanic warming. *Nature communications*, 10(1), 205,
852 <https://doi.org/10.1038/s41467-018-08066-0>, 2019.
- 853 • Retailleau, L., & Gualtieri, L. Toward high-resolution period-dependent seismic
854 monitoring of tropical cyclones. *Geophysical Research Letters*, 46(3), 1329-1337,
855 <https://doi.org/10.1029/2018GL080785>, 2019.
- 856 • Retailleau, L., & Gualtieri, L. Multi-phase seismic source imprint of tropical cyclones.
857 *Nature communications*, 12(1), 2064, <https://doi.org/10.1038/s41467-021-22231-y>,
858 2021.



- 859 • Rost, S., & Thomas, C. Array seismology: Methods and applications. *Reviews of*
860 *geophysics*, 40(3), 2-1, <https://doi.org/10.1029/2000RG000100>, 2002.
- 861 • Rumora, I., Jukić, O., Filić, M., & Filjar, R. A study of GPS positioning error associated
862 with tropospheric delay during Numa Mediterranean cyclone. *Int J for Transp and Traff*
863 *Eng*, 8(3), 282-293, [https://doi.org/10.7708/ijtte.2018.8\(3\).03](https://doi.org/10.7708/ijtte.2018.8(3).03), 2018.
- 864 • Sarpkaya, T., & Isaacson, M. Mechanics of wave forces on offshore structures Van
865 Nostrand Reinhold Company New York. *New York*, 1981.
- 866 • Saviano, S., Kalampokis, A., Zambianchi, E., & Uttieri, M. A year-long assessment of
867 wave measurements retrieved from an HF radar network in the Gulf of Naples
868 (Tyrrhenian Sea, Western Mediterranean Sea). *Journal of Operational Oceanography*,
869 12(1), 1-15, <https://doi.org/10.1080/1755876X.2019.1565853>, 2019.
- 870 • Scardino, G., Scicchitano, G., Chirivì M., Costa P.J.M., Luparelli A., Mastronuzzi G.
871 Convolutional Neural Network and Optical Flow for the Assessment of Wave and Tide
872 Parameters from Video Analysis (LEUCOTEIA): An Innovative Tool for Coastal
873 Monitoring. *Remote Sensing*, 14, 2994, doi.org/10.3390/rs14132994, 2022.
- 874 • Scicchitano, G., Scardino, G., Monaco, C., Piscitelli, A., Milella, M., De Giosa, F., &
875 Mastronuzzi, G. Comparing impact effects of common storms and Medicanes along the
876 coast of south-eastern Sicily. *Marine Geology*, 439, 106556,
877 <https://doi.org/10.1016/j.margeo.2021.106556>, 2021.
- 878 • Shaltout, M., & Omstedt, A. Recent sea surface temperature trends and future scenarios
879 for the Mediterranean Sea. *Oceanologia*, 56(3), 411-443, [https://doi.org/10.5697/oc.56-](https://doi.org/10.5697/oc.56-3.411)
880 3.411, 2014.
- 881 • Soubestre, J., Shapiro, N. M., Seydoux, L., de Rosny, J., Droznin, D. V., Droznina, S.
882 Y., ... & Gordeev, E. I. Network-based detection and classification of seismovolcanic
883 tremors: Example from the Klyuchevskoy volcanic group in Kamchatka. *Journal of*



- 907 • Zhang, J., Gerstoft, P., & Bromirski, P. D. Pelagic and coastal sources of P-wave
908 microseisms: Generation under tropical cyclones. *Geophysical Research Letters*,
909 37(15), <https://doi.org/10.1029/2010GL044288>, 2010.
- 910 • Zimbo, F., Ingemi, D., & Guidi, G. The tropical-like cyclone “ianos” in September
911 2020. *Meteorology*, 1(1), 29-44, <https://doi.org/10.3390/meteorology1010004>, 2022.

912

913

914

915

916

917 **Authors Contribution**

918 A.M.B., A.C. and F.C. conceived the idea. A.M.B. analyzed seismic data and V.M. performed
919 array analysis. C.L.R, G.N., A.O. and M.P. analyzed buoys data. S.A., D.C., G.D.G., G.L.,
920 S.D., R.D. and T.L. helped perform seismic analysis. F.C., G.C., S.A., I.F., G.G. G.M.,
921 analyzed HF Radar Data. A.M.B. and V.M. wrote the paper. S.A., F.C., D.C., G.L. and V.M.
922 dealt with the new seismic installation. G.C. lead one of the projects funding this research, G.S.
923 helped to interpret the sea state data. All the authors discussed the results, edited the paper and
924 gave consent for this publication under the supervision of A.C.

925

926

927

928

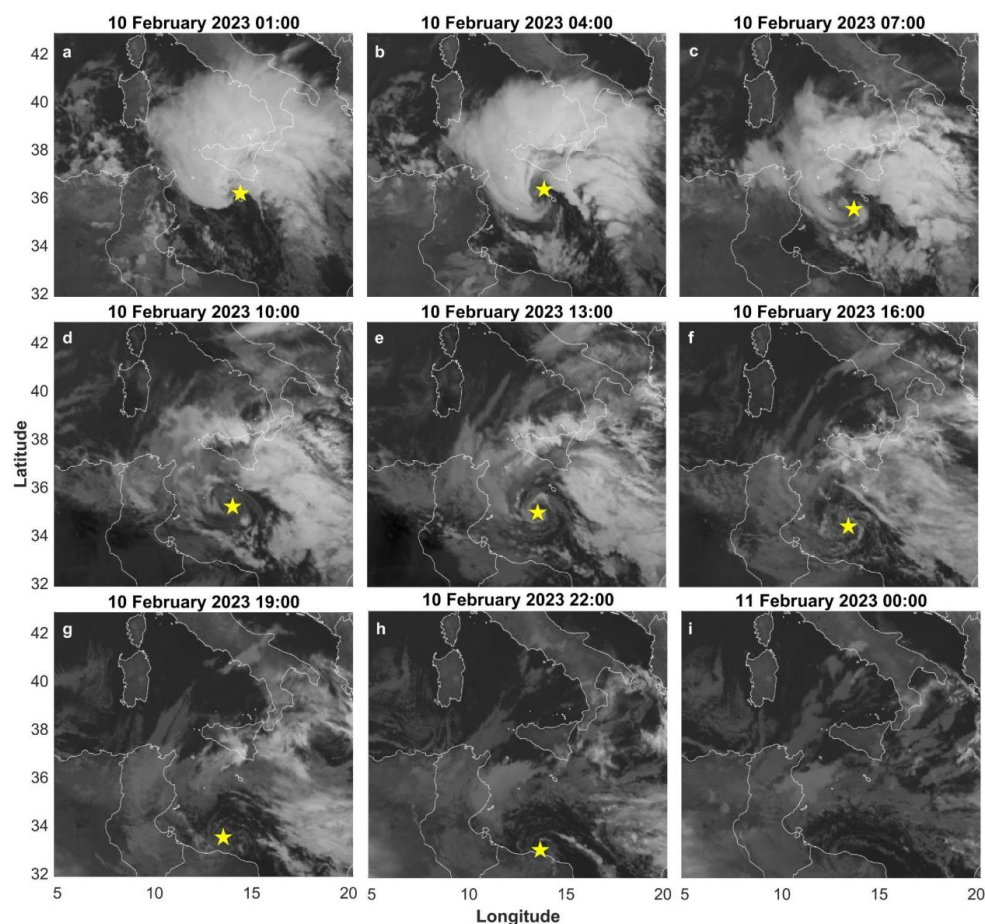
929

930

931



932 **Figures**



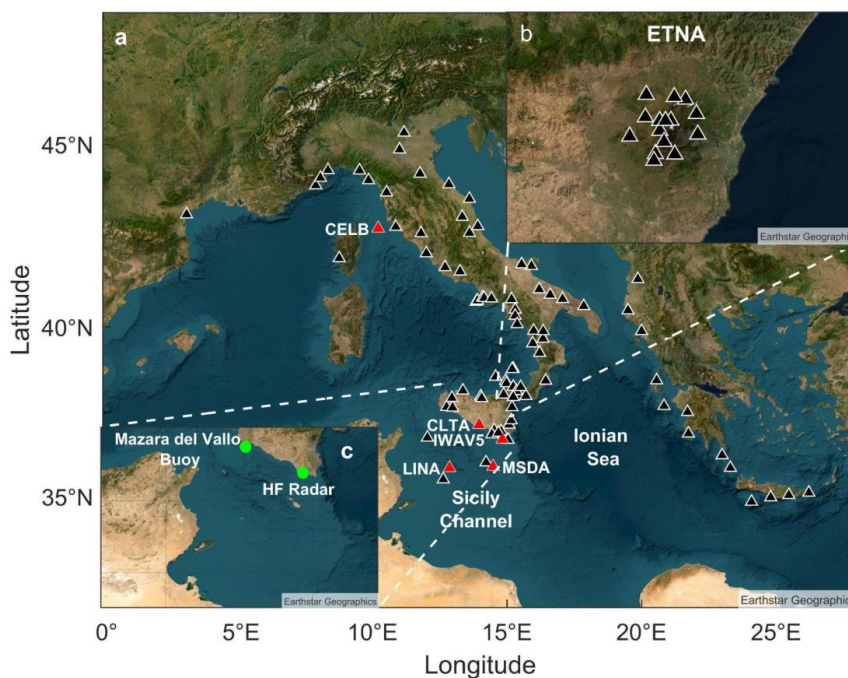
933

934 **Figure 1:** Satellite images of the Mediterranean area and of the sub-tropical system Helios

935 during the period 10/02/2023 01:00 - 11/02/2023 00:00. The yellow stars in (a-h) show the

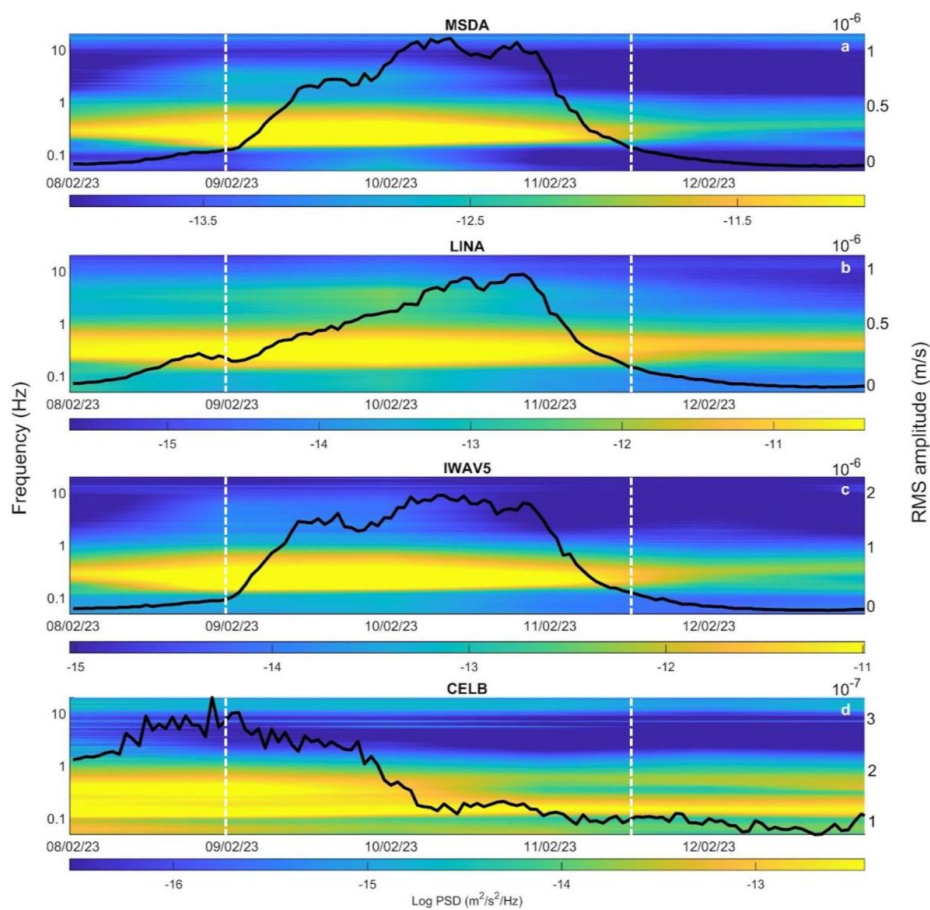
936 position of the cyclone eye. The lack of the star in (i) is due to the dissipation of Helios after

937 the landfall against the Libyan coast (h). (©EUMETSAT SEVIRI Images)



938

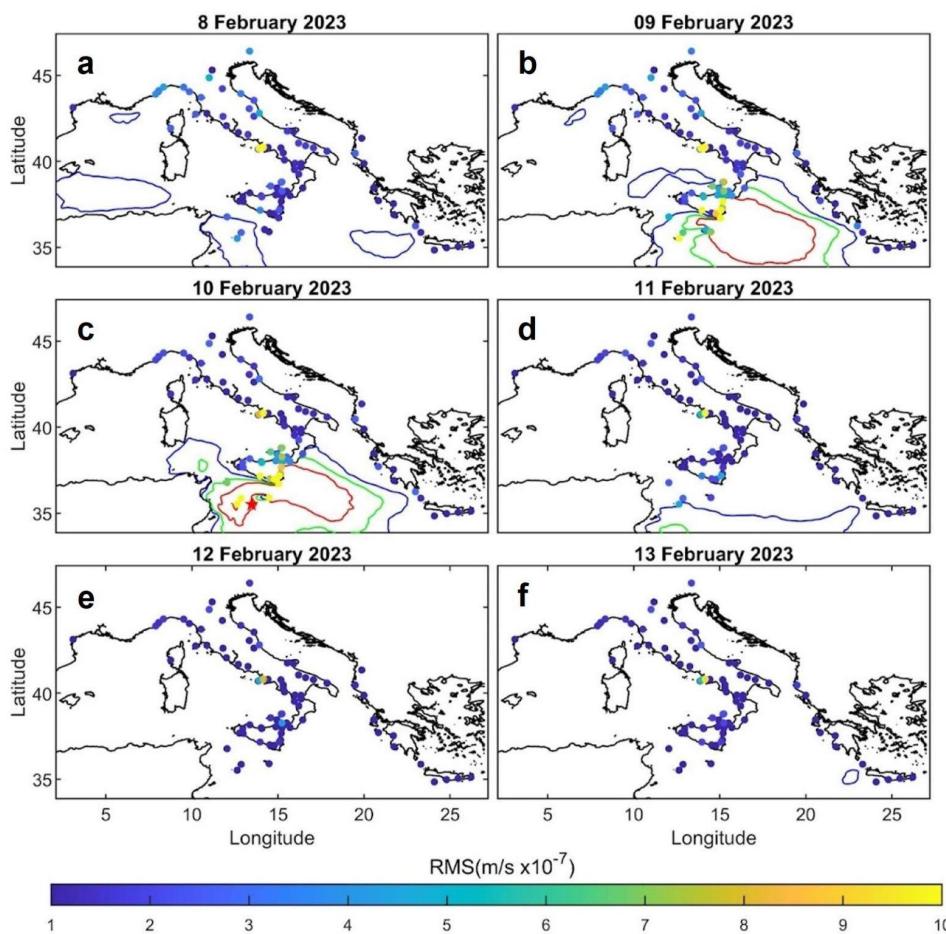
939 **Figure 2:** Satellite image of the Mediterranean area with a selection of the broadband seismic
940 stations available in the ORFEUS and INGV databases and used in the spectral analysis and in
941 the grid search method (a) and selection of the broadband seismic stations in the Etna area
942 maintained by INGV-OE (b), used in the array analysis (base image source ©Earthstar
943 Geographic). The red triangles indicate the stations used in the detailed analysis shown in
944 Figures 3 and 9 and in **Supplementary Figures 1 and 2**. The green dots in (c) indicate the
945 position of the wavemeter buoy (Mazara del Vallo) and of the HF Radar (Marina di Ragusa)
946 used for the sea state monitoring.



947

948 **Figure 3:** Spectrograms and RMS amplitude time series for the SM band (0.1-0.2 Hz) of the
949 seismic signal recorded by the vertical component of 4 stations located along the Maltese
950 coastline (a), in Linosa Island (b), in the southern part of Sicily (c) and in Central Italy (d) (see
951 **Figure 2a** for the station locations).

952



953

954 **Figure 4:** Spatial and temporal distribution of the RMS amplitude for the SM band computed

955 at the 105 stations considered (dots). The colors of dots represent the RMS amplitude as

956 specified in the color bar. The blue, green and red contour lines represent significant wave

957 heights of 3, 4 and 5 m, respectively, while the red five-point star in (c) indicates the eye

958 position of the sub-tropical system Helios obtained from satellite images.

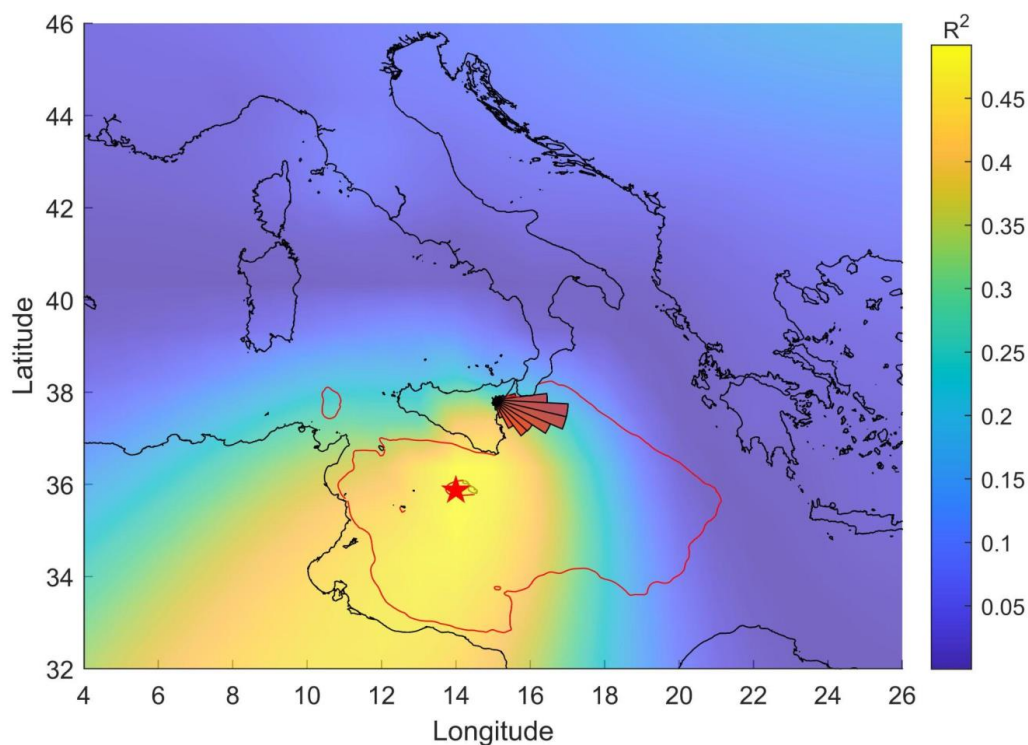
959

960

961

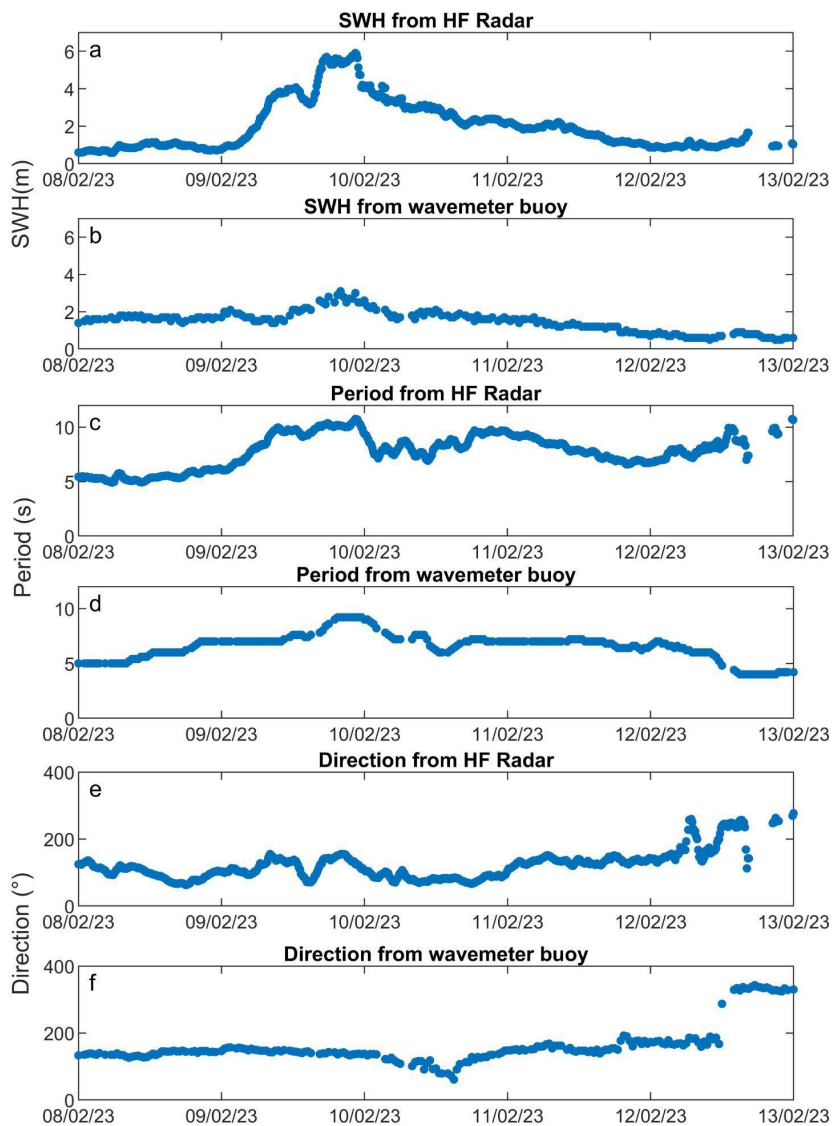
962

963



964

965 **Figure 5:** Localization of the microseism source for 10 February 2023 at 16:00. The red five-
966 point star indicates the centroid position of all the grid nodes whose R^2 values do not differ by
967 more than 1% from the maximum R^2 value obtained with the grid search method, while the
968 rose diagram, located at the center of the summit area of Mt. Etna (see **Figure 2b**), shows the
969 distribution of the back azimuth values on the same day. The red contour line represents
970 significant wave heights of 4 m obtained from the Copernicus product
971 MEDSEA_HINDCAST_WAV_006_012 during the same time interval.

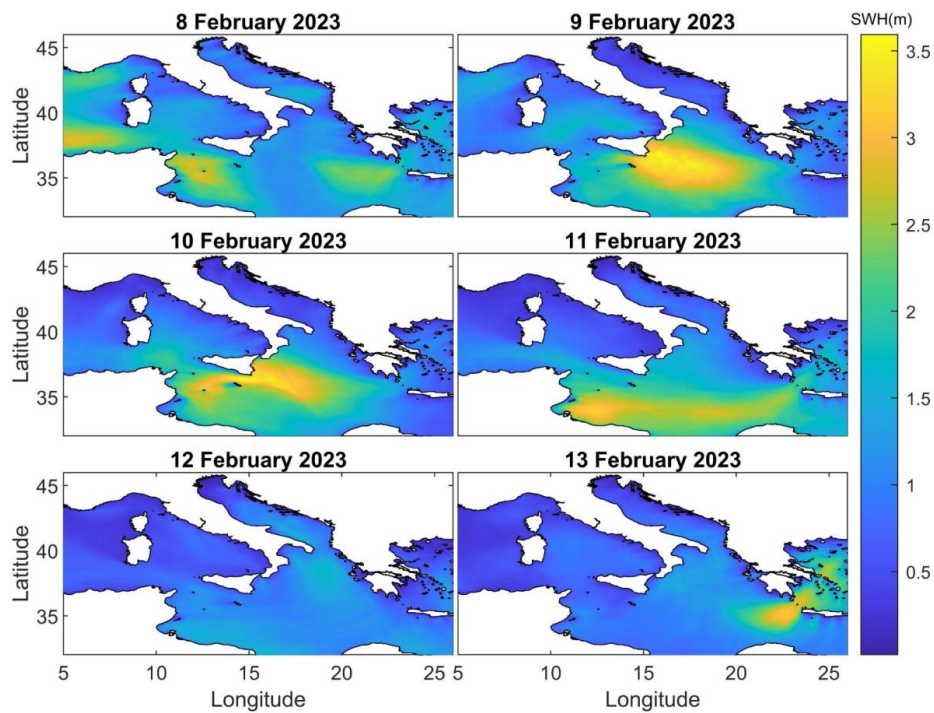


972

973 **Figure 6:** Wave features in terms of SWH, period and mean direction time series retrieved by

974 using the HF Radar (a, c and e) and Mazara del Vallo buoy (b, d and f) data. For the instruments

975 location see **Figure 2c**.

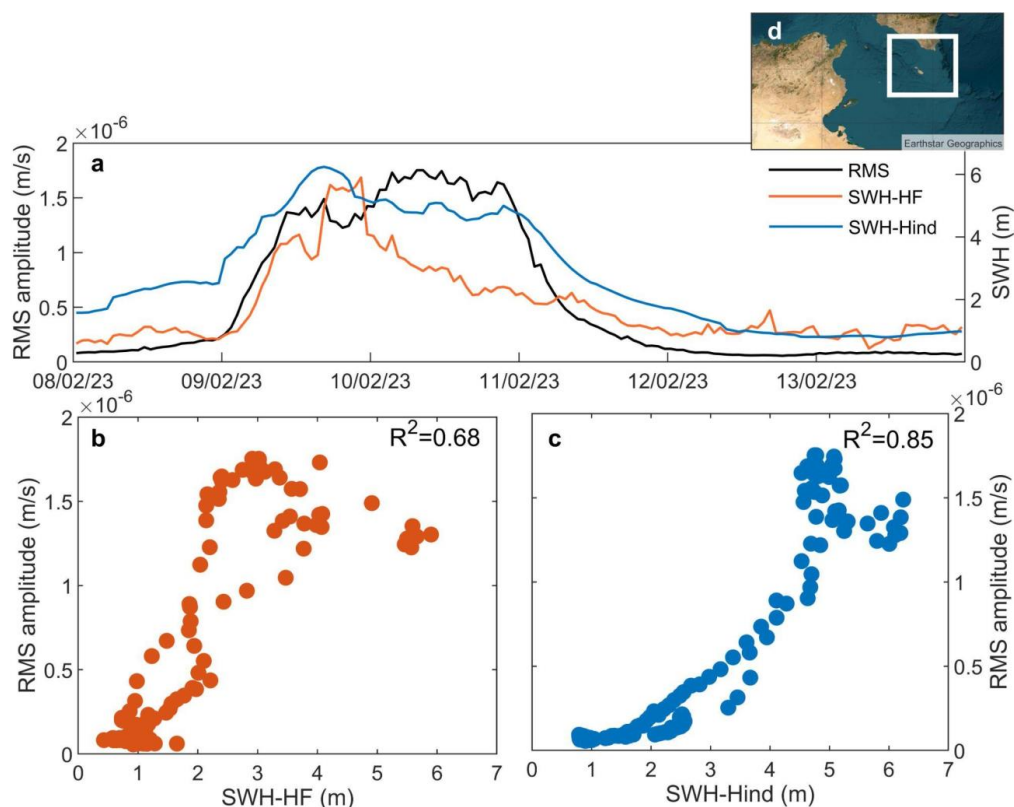


976

977 **Figure 7:** Hindcast maps, obtained from the Copernicus product

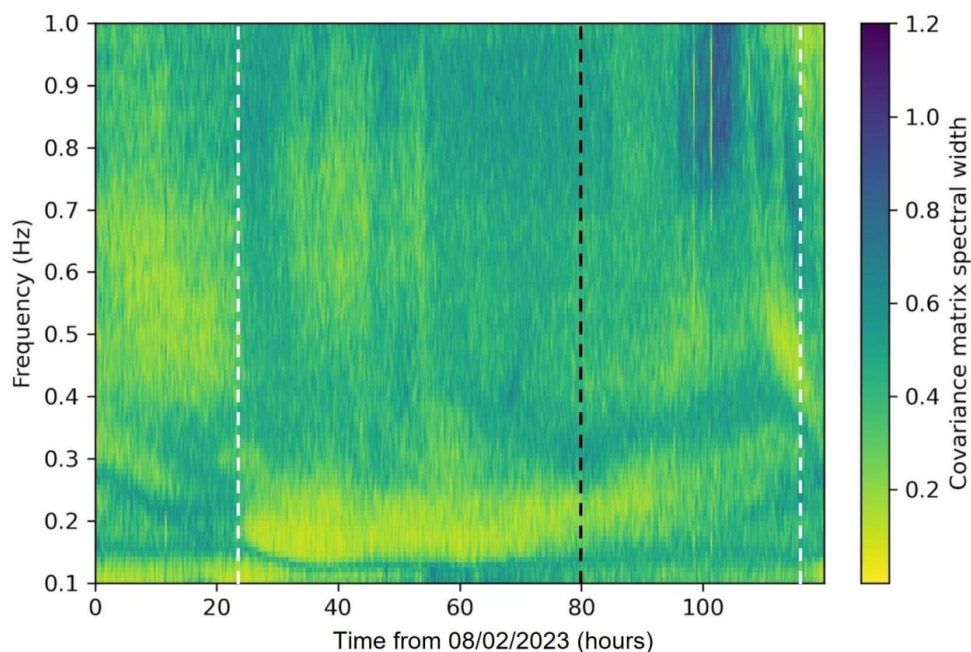
978 MEDSEA_HINDCAST_WAV_006_012, showing the spatio-temporal variations of SWH

979 during the days taken into account.



980

981 **Figure 8:** (a) RMS amplitude time series, recorded at the station IWAV5, and SWH time series
 982 retrieved by HF Radar (SWH-HF; orange line) and by hindcast data (SWH-Hind; light-blue).
 983 Cross-plot showing the relation between SWH-HF and RMS amplitude (b) and between SWH-
 984 Hind and RMS amplitude (c). The value of the determination coefficient (R^2) is reported in the
 985 upper right corner of the plots (b) and (c). In (d) the area of the Sicily Channel used to calculate
 986 the SWH-Hind time series is shown (base image source ©Earthstar Geographic). For the
 987 instruments location see **Figure 2a** and **2c**.



988

989 **Figure 9:** Covariance matrix spectral width obtained for the period 8-12 February 2023 using
990 the stations IWAV5, LINA, MSDA and CLTA. The white dashed lines represent the
991 development and the ending of the sub-tropical system Helios, while the black dashed line
992 indicates the time when Helios makes landfall against the Libyan coast. For stations location
993 see **Figure 2a**.

994

995

996

997



998 Table

Date	Hour	Longitude of microseim source (degrees)	Latitude of microseism source (degrees)	R ² Value	Longitude of cyclone eye from satellite data (degrees)	Latitude of cyclone eye from satellite data (degrees)
09/02/2023	08:00	15.0000	37.3681	0.3233	/	/
09/02/2023	12:00	15.0000	36.3681	0.3459	/	/
09/02/2023	16:00	15.0000	36.3681	0.3554	/	/
09/02/2023	20:00	15.0000	36.3681	0.3865	/	/
10/02/2023	00:00	14.5000	36.3681	0.4725	/	/
10/02/2023	04:00	14.5000	36.3681	0.5066	14.01584	36.24165
10/02/2023	08:00	14.3030	36.0348	0.5107	13.79612	35.57149
10/02/2023	12:00	14.3030	36.0348	0.5091	13.91697	35.13203
10/02/2023	16:00	14.0000	35.8681	0.4920	13.59836	34.5937
10/02/2023	20:00	14.0000	35.8681	0.4762	13.52146	33.59395
11/02/2023	00:00	14.0000	35.8681	0.3864	13.74118	32.9897



999 **Table 1.** Main features of the microseism sources and comparison with the coordinates of the
1000 cyclone eye retrieved from satellite data. The coordinates of the cyclone eye between 8:00 of
1001 9 February and 00:00 of 10 February are absent since the cyclone eye is clearly visible
1002 between 01:00 and 23:00 of 10 February 2023.